Large-Scale SST Variability in the Western North Atlantic Subtropical Convergence Zone during FASINEX. Part I: Description of SST and Wind Stress Fields*

GEORGE R. HALLIWELL, JR. AND PETER CORNILLON

Graduate School of Oceanography, University of Rhode Island, Narragansett, Rhode Island

(Manuscript received 20 July 1988, in final form 18 August 1989)

ABSTRACT

We describe properties of large-scale fluctuations in the wind field represented by two analyses (FNOC and NOAA ATOLL), and in the SST field represented by maps derived from 5-day composite AVHRR images, within an 11° longitude by 10° latitude domain during FASINEX (January through June 1986). FNOC and ATOLL wind and wind stress time series were highly correlated with each other (>0.8) over the entire domain, and they were also highly correlated with time series measured at the FASINEX site ≥ 0.89. At periods of 2–13 days, clockwise $\bar{\tau}$ energy exceeded anticlockwise energy by an order of magnitude, while the energy was nearly partitioned equally at periods of 13–40 days. Mean ATOLL winds were everywhere more eastward than mean FNOC winds, probably in part because the ATOLL (FNOC) analyses are intended to represent 850 mb (19.5 m) winds. The 850 mb winds are expected to be more eastward due to the thermal wind balance with the mean southward air temperature gradient. The SST maps represented large-scale variability with reasonable accuracy, although a mean positive SST bias of about 0.5–0.6°C resulted from the image compositing procedure. This bias did not seriously affect the ability to detect either large-scale SST features or frontal zones in the 5-day maps. A single frontal zone up to 3° of latitude wide, which crossed the domain in a predominantly zonal direction, was the dominant large-scale frontal feature in the SST maps. Perturbations in the strength of this frontal zone shifted westward at several kilometers per day.

1. Introduction

The oceanic subtropical convergence zone (STCZ) in the Northern Hemisphere is the latitude band typically centered between about 22° and 32°N where strong meridional convergence of wind-driven meridional Ekman transport exists between the westerlies to the north and the trade winds to the south. One or more surface oceanic fronts are usually observed within this band, distinguished by temperature jumps of 1–3°C within a distance of several kilometers (Voorhis 1969; Van Woert 1982). Since the meridional gradient in the solar heat flux at middle latitudes tends to produce a T_s field dominated by very large meridional scales, horizontal gradients of either horizontal heat flux within the mixed layer or vertical heat fluxes through the surface and base of the mixed layer are necessary for these fronts to form. Since the meridional convergence of Ekman transport will tend to cause the zonally oriented T_s isotherms to converge within the STCZ, it is usually considered to be the primary mech-

anism responsible for the existence of strong fronts within the STCZ (e.g., Roden 1975).

The Frontal Air-Sea Interaction Experiment (FASINEX) was designed to study air–sea interaction processes at an open-ocean front, and the intensive phase of this experiment was conducted within the STCZ southwest of Bermuda between January and June 1986 (Stage and Weller 1985, 1986). Although the measurement program was designed primarily to sample atmospheric and oceanic variability near a subtropical front at scales < 100 km, the experiment included a component to describe larger-scale variability in the FASINEX region. Two primary goals of this component were to describe the large-scale background variability within which FASINEX measurements were embedded, and to identify and quantify the processes acting at large scales that generate the strong fronts observed in the FASINEX region.

To achieve these goals, we analyzed the variability of T_s and fronts at wavelengths of O(1000) km (henceforth referred to as large-scale variability) in the FASINEX region using T_s maps derived from AVHRR images along with wind analysis fields. In this paper, we describe the processing of the wind and T_s fields used in these analyses, evaluate the quality of these fields by comparing them to measurements at the FASINEX moorings, then briefly describe some basic statistical properties of the wind stress, wind stress curl,

* FASINEX Contribution Number 60.

Corresponding author address: Dr. George R. Halliwell, Graduate School of Oceanography, University of Rhode Island, Narragansett, RI 02882.

and T_s fields at large scales. This sets the stage for the quantitative analyses designed to assess the influence of wind-driven horizontal heat advection on T_s and frontal variability that is presented in Halliwell and Cornillon (1990, henceforth referred to as Part II).

2. The data

Using AVHRR/2 images from NOAA-7 and NOAA-9 satellites, we derived 5-day maps of T_s from January through June 1986 on a 0.25 × 0.25 grid (referred to as the T_s grid) within a domain bounded by 22.625–32.375°N and 72.625–61.375°W (Fig. 1). We obtained NOAA ATOLL (Analysis of Tropical Ocean Lower Layer) wind analyses from the National Hurricane Center, and also obtained marine wind analyses (Lewis and Grayson 1972; Friehe and Pazan 1978) from the Fleet Numerical Oceanography Center (FNOC), on the grid points shown in Fig. 1 at 0000 and 1200 UTC daily between 1 January and 30 June 1986. The 8 × 8 ATOLL grid has a longitude spacing of 1.5° and a latitude spacing of about 1.4°, the latter adjusted to equalize the grid point separation in x and y. The 5 × 5 FNOC grid is part of the 144 × 73 global spherical grid and has a uniform longitude and latitude spacing of 2.5°. The ATOLL winds are produced by objective analysis of land, ship, rawinsonde, and satellite cloud winds, and are intended to represent 850 mb winds (just above the planetary boundary layer). The FNOC winds are calculated from surface atmo-

spheric pressure analyses using the gradient wind equation, then statistically/dynamically adjusted to represent 19.5 m winds by the Numerical Variational Analysis technique using a model that includes frictional effects in the surface boundary layer (Lewis and Grayson 1972).

We also obtained hourly wind and T_s time series from surface buoys at FASINEX moorings F2, F4, F6, F8, and F10 (Fig. 1; Pennington et al. 1988) that do not quite span the entire six-month interval (Table 1). We obtained FASINEX ship-of-opportunity XBT data (Evans et al. 1986; Halliwell 1990) to compare the spatial variability of satellite-derived T_s to the spatial variability of XBT-derived T_s.

Considerable processing was required to remove the effects of clouds from the AVHRR images and grid the T_s maps. To begin with, the data were subsampled by selecting the warmest pixel in each 4 × 4 pixel square. The resulting fields, still in satellite coordinates, were scan-angle corrected (Cornillon et al. 1987) to compensate for the decreased radiation reaching the spacecraft at large scan angles due to the increased path length through the atmosphere. All images were then re-mapped to a 512 × 512 array centered at 27.5°N, 67°W with a grid spacing of 0.0226° in longitude and 0.0200° in latitude. All images within each five day interval were then composited (the warmest temperature at each pixel was selected) to form a single image for each interval between 1 to 5 January and 30 June to 4 July. All pixels where the temperature was less
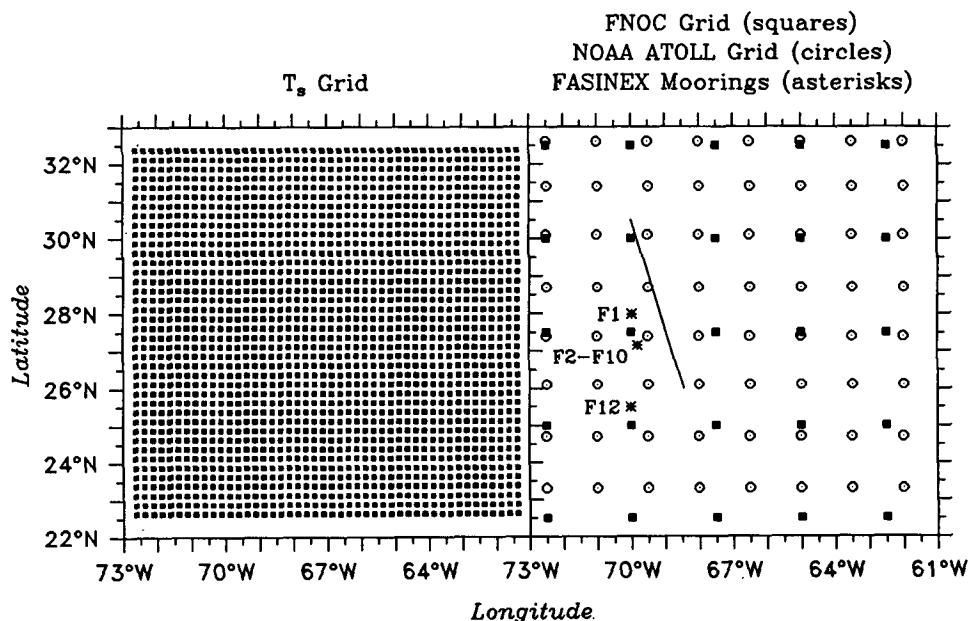

FIG. 1. Points of the T_s grid (left), points of the NOAA ATOLL (circles, right) and FNOC (squares, right) grids, and the location of FASINEX moorings (asterisks, right). The straight line in the right panel shows the approximate path of the ship-of-opportunity XBT cross-sections used in Fig. 10. For each NX × NY grid, the point (1, 1) is located at the southwest corner and the point (NX, NY) is located at the northeast corner.

TABLE 1. The location of the FASINEX surface buoys and the start and end times (UTC, all during 1986) of the 6-h and 5-day $\bar{\tau}$ and T_s time series measured at the buoys.

Buoy	Lat. (N)	Long. (W)	6-h time series		5-day time series	
			Start	End	Start	End
F2	27.32°	70.10°	1200 UTC 18 Jan	1800 UTC 11 Jun	21–25 Jan	5–9 Jun
F4	27.09	69.84	1200 UTC 19 Jan	0600 UTC 13 Jun	21–25 Jan	5–9 Jun
F6	27.21	69.97	1200 UTC 29 Jan	0600 UTC 12 Jun	31 Jan–4 Feb	5–9 Jun
F8	26.98	69.72	1200 UTC 30 Jan	0000 UTC 13 Jun	31 Jan–4 Feb	5–9 Jun
F10	27.33	69.71	1200 UTC 4 Feb	1200 UTC 7 Jun	5–9 Feb	31 May–4 Jun

than 18.5°C were then flagged as cloud-contaminated. Additional pixels that could be contaminated by clouds were identified by comparing temperatures from each five-day composite image to temperatures from a composite of both the preceding and following five-day composite images. Pixels where the temperature differed by more than 1.25°C were assumed to be influenced by clouds. All regions flagged as cloud-contaminated were then expanded by one pixel in both the x and y directions to increase the certainty that the edges of cloud-influenced regions were flagged. All flagged pixels (more than one-third) were then discarded. The first and last of the five-day images were discarded due to the above procedure, so the final dataset spanned the time interval 6–10 January through 25–29 June 1986.

The T_s estimates were then binned and averaged onto a grid with 0.25° resolution in both latitude and longitude (Fig. 1), selected to maintain as high a resolution as possible while minimizing the number of grid points without data. Some of the resulting T_s maps were nearly complete (<2% missing data), while a few maps were substantially less so (up to 20% missing data). For all 35 maps, an average of 5.2% of the data was missing. For the time series of T_s at each grid point, all gaps of one five-day interval in length were filled using cubic spline interpolation in time. This step reduced the percentage of missing data values to 1.6. The remaining gaps in each map were filled in the space domain. For each grid point with missing data, a fifth-order polynomial function was fit to all available good data on a subset of surrounding grid points, then was used to estimate T_s. Contour plots of the resulting T_s maps, along with other fields derived from these maps, are presented in Halliwell and Cornillon (1987).

Winds for the four ATOLL analyses that were missing between January and June 1986 were filled by cubic spline interpolation in time. We then calculated wind stress $\bar{\tau} = (\tau^{(x)}, \tau^{(y)})$ for both wind analysis fields along with the FASINEX buoy winds using the bulk aerodynamic formula with drag coefficient calculated by the empirical equation of Large and Pond (1981). Since this formula requires winds measured 10 m above the surface, while wind sensors at the FASINEX buoys were located 3.5 m above the surface, measured winds

were adjusted to represent 10 m winds assuming that the atmosphere was neutrally stable (Halliwell et al. 1986). We used these adjusted measured winds in all subsequent analyses. Although the ATOLL winds are intended to represent 850 mb winds (near the top of the atmospheric boundary layer) and the FNOC winds are intended to represent 19.5 m winds, we did not adjust the amplitudes of the ATOLL and FNOC winds to 10 m because they were already nearly equal to the amplitudes of the 10 m winds at the FASINEX buoys (section 3a). The ATOLL analyses may therefore underestimate the magnitude of the 850 mb winds. Complex correlation analysis (section 3a) revealed that the FNOC and ATOLL vector wind fluctuations were aligned both with each other and with FASINEX measured vector wind fluctuations. Consequently, a rotation correction was not applied to the analyzed wind fields. This was a bit surprising because 850 mb winds should be rotated clockwise from near-surface winds due to Ekman veering.

We low-pass filtered (40-h half-amplitude point) all wind and wind stress time series, as well as all T_s time series, measured at the FASINEX buoys, then decimated them to 0000, 0600, 1200, and 1800 UTC for each day. The start and end times of the filtered buoy records are listed in Table 1. Since the FNOC and ATOLL wind analyses were 12-hourly, we used cubic spline interpolation in time to generate six-hourly analyses at the sampling times of the filtered buoy records. Wind stress curl ($\mathbf{k} \cdot \nabla \times \bar{\tau}$) maps were then calculated using the following centered first-difference formula to determine the x and y derivatives:

$$f'_0 = \frac{1}{12h^2}(-f_{-2} + 16f_{-1} - 30f_0 + 16f_1 - f_2), \quad (1)$$

where f is an arbitrary function, the prime signifies derivative, and h is the separation distance. These maps were calculated at the ATOLL and FNOC grid points shown in Fig. 1 using additional grid points surrounding the domain that are not shown. We then low-pass filtered the six-hourly FNOC and ATOLL wind and wind stress curl time series.

Finally, we averaged all filtered time series over the 5-day intervals of the satellite-derived T_s maps, and the

TABLE 2. The FNOC and ATOLL grid points, along with the six T_s grid points, that are located closest to the FASINEX buoys and used in our wind and T_s quality evaluations. Refer to Fig. 1 for the grid point numbering convention.

Grid point	Longitude (W)	Latitude (N)
FNOC (2, 3)	70.00°	27.32°
ATOLL (3, 4)	69.50	27.09
T_s (11, 19)	70.125	27.125
T_s (12, 19)	69.875	27.125
T_s (13, 19)	69.625	27.125
T_s (11, 20)	70.125	27.375
T_s (12, 20)	69.875	27.375
T_s (13, 20)	69.625	27.375

start and end times of the resulting 5-day buoy series are listed in Table 1. We refer to the low-pass filtered and the 5-day averaged time series as 6-h and 5-day time series, respectively.

3. The wind and wind stress fields

a. Quality evaluation

We evaluate the quality of the two wind analyses by directly comparing time series of wind and wind stress at the FNOC and ATOLL grid points closest to the FASINEX buoys (Tables 1 and 2) with time series measured at those buoys. We evaluate both 6-h and 5-day time series since we use the latter to perform the analyses described in Part II. Mean wind and wind stress calculated from the 6-h time series are much smaller than the rms amplitudes (Table 3). The mean values of both v and $\tau^{(y)}$ do not significantly differ (to 95% confidence) among the five buoys and two analyses. The mean values of both u and $\tau^{(x)}$ are not significantly different among the five buoys and the FNOC analysis, but mean values of ATOLL u and $\tau^{(x)}$ both have a larger eastward component than either the FNOC analysis or the FASINEX measurements. As a result, mean FNOC and buoy $\bar{v}$ all have magnitudes near 0.45 m s^{-1} and point toward the north and north-

east (Table 3), while mean ATOLL $\bar{v}$ has a magnitude of 1.38 m s^{-1} and points just north of due east. Despite the differences in the means, components of both $\bar{v}$ and $\bar{\tau}$ from all sources have very similar rms amplitudes. For this reason, we did not adjust the magnitudes of the FNOC and ATOLL winds to 10 m elevation (section 2).

Complex correlation coefficients among FNOC-measured, ATOLL-measured, and FNOC-ATOLL time series of 6-h $\bar{v}$, 6-h $\bar{\tau}$, and 5-day $\bar{\tau}$ all range from 0.89–0.95 (Table 4). Similar correlation magnitudes are observed whether individual buoy time series or spatial averages over all five buoys are compared to the FNOC and ATOLL time series. The correlation magnitudes among pairs of FASINEX buoys are larger, ranging from 0.96–0.99 (Table 4). Phase angles are all within a few degrees of zero, which is why we did not apply a rotation correction to the FNOC and ATOLL winds (section 2). Fluctuations in wind and wind stress are quite well represented by the two wind analyses, despite the fact that they represent wind that has been effectively smoothed over a space scale of several hundred kilometers (e.g., Halliwell and Allen 1987). This may result in part because much of the smaller-scale wind variability, such as the variability near atmospheric fronts, is energetic at periods < 2 days and is therefore reduced substantially by the temporal filtering.

Plots of 5-day $\tau^{(x)}$ and $\tau^{(y)}$ from FASINEX buoy F2, along with 5-day ATOLL and FNOC time series from the nearest grid points (Fig. 2), illustrate the strong similarities in the fluctuations among these time series. The differences between ATOLL mean $\tau^{(x)}$ and the other means of $\tau^{(x)}$ are evident, but they are much smaller than the magnitude of the fluctuations. The correlation between the FNOC and ATOLL wind stress curl time series plotted in Fig. 2 (0.46) is substantially smaller than the wind stress correlations (Table 4).

Spectrum analysis was performed to study how well the two wind sets represent $\bar{\tau}$ and $\mathbf{k} \cdot \nabla \times \bar{\tau}$ variability as a function of frequency. Spectrum functions were calculated using 6-h time series from the same moor-

TABLE 3. Mean wind and wind stress for the FNOC and ATOLL grid points closest to the FASINEX buoys, and for the individual FASINEX buoys. Rms amplitudes are shown in parentheses. Differences of 0.19 (0.25) m s^{-1} in mean winds are statistically significant to 95% (99%) confidence. The corresponding minimum significant differences for wind stress components are 0.30 (0.41) Pa. Angles are measured anticlockwise from due east. Statistics are calculated using 6-h time series over the interval 4 February through 7 June common to all records.

Buoy/wind analysis	$|\bar{v}|$ (m s^{-1})	θ (deg)	u (m s^{-1})	v (m s^{-1})	$\tau^{(x)}$ ($\times 10^2$ Pa)	$\tau^{(y)}$ ($\times 10^2$ Pa)
FNOC (2, 3)	0.40	62	0.19 (4.73)	0.35 (4.43)	0.31 (6.65)	0.44 (6.05)
ATOLL (3, 4)	1.38	5	1.38 (5.06)	0.11 (4.15)	2.23 (7.15)	0.21 (5.67)
F2	0.42	56	0.24 (5.03)	0.35 (4.74)	0.75 (7.99)	0.39 (7.12)
F4	0.48	92	−0.02 (4.93)	0.48 (4.61)	0.35 (7.60)	0.51 (6.66)
F6	0.45	78	0.09 (5.00)	0.44 (4.69)	0.54 (7.91)	0.47 (7.02)
F8	0.40	89	0.01 (4.90)	0.40 (4.47)	0.34 (7.42)	0.39 (6.27)
F10	0.47	84	0.05 (5.21)	0.47 (4.70)	0.58 (8.20)	0.50 (6.95)

TABLE 4. Complex correlation coefficients among 6-h and 5-day time series of wind and wind stress from the FNOC and ATOLL grid points closest to the FASINEX buoys, for the individual FASINEX buoys, and for time series averaged over the five FASINEX buoys. For comparison, complex correlation coefficients between F2 and other FASINEX buoys are also presented. All correlations are calculated over the entire common record length for each pair of time series.

		Magnitude			Phase (deg)		
Series 1	Series 2	$\vec{v}$ (6-h)	$\vec{\tau}$ (6-h)	$\vec{\tau}$ (5-day)	$\vec{v}$ (6-h)	$\vec{\tau}$ (6-h)	$\vec{\tau}$ (5-day)
FNOC	F2	0.93	0.92	0.93	1.7	2.9	−2.7
ATOLL	F2	0.89	0.89	0.92	5.6	5.7	3.9
FNOC	F4	0.92	0.92	0.90	5.2	6.6	−5.9
ATOLL	F4	0.89	0.89	0.90	8.6	8.9	1.7
FNOC	F6	0.93	0.92	0.93	2.4	3.2	2.7
ATOLL	F6	0.89	0.89	0.92	6.5	6.4	6.3
FNOC	F8	0.91	0.91	0.91	0.5	1.5	−0.4
ATOLL	F8	0.89	0.89	0.91	4.2	4.4	3.0
FNOC	F10	0.92	0.91	0.92	−1.0	−0.4	−0.1
ATOLL	F10	0.89	0.89	0.92	3.1	2.6	3.4
FNOC	F2–F10 Avg	0.92	0.92	0.95	1.0	1.9	2.4
ATOLL	F2–F10 Avg	0.89	0.89	0.94	5.3	5.2	5.9
FNOC	ATOLL	0.90	0.89	0.91	−4.3	−3.6	−5.5
F2	F4	0.99	0.99	0.97	3.7	3.7	−2.5
F2	F6	0.99	0.99	0.97	1.7	1.7	−0.1
F2	F8	0.98	0.98	0.96	−0.1	0.1	−3.1
F2	F10	0.98	0.98	0.97	−0.9	−1.2	−2.5

ings and grid points as the 5-day time series plotted in Fig. 2. These functions were band-averaged in the frequency domain to yield 14 degrees of freedom, resolving 11 frequency bands between 0.028 and 0.5 cpd. Rotary autospectra (Mooers 1973) of $\vec{\tau}$ are graphed for both the clockwise and anticlockwise components in Fig. 3. The spectral shapes are not significantly dif-
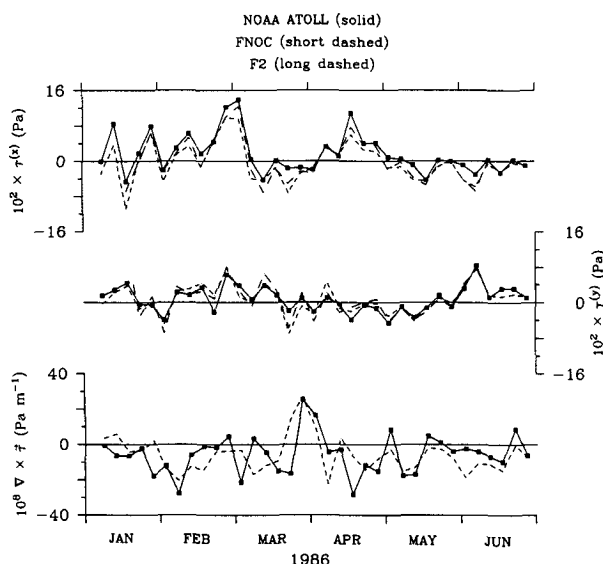

FIG. 2. Five-day averaged $\vec{\tau}$ components measured at FASINEX buoy F2 (long dashed) and analyzed at the nearest ATOLL (solid) and FNOC (short dashed) grid points listed in Table 2 (top and center). Also shown are ATOLL (solid) and FNOC (short dashed) $k \cdot \nabla \times \vec{\tau}$ from the same grid points (bottom).

ferent among the FNOC, ATOLL, and buoy F2 time series. In all time series, the clockwise and anticlockwise components have about the same energy for the two lowest frequency bands resolved (0.028 and 0.077 cpd), but the clockwise energy is an order of magnitude larger than the anticlockwise energy at higher frequencies. The anticlockwise spectra roughly decrease monotonically with increasing frequency while the clockwise spectra have a statistically insignificant peak near 0.18 cpd. The scalar autospectra for FNOC and ATOLL wind stress curl (Fig. 3) are substantially more white than the $\vec{\tau}$ spectra.

The dominance of clockwise variance is evident in the plot of surface vector wind at F2 during March 1986 (Fig. 4). Three distinct events occurred during this month where the vector wind rotated clockwise nearly 360 degrees: 7–11, 17–20, and 23–27 March. A number of similar events occurred during the other months, and they basically resulted from the repeated passage of cold fronts followed by anticyclones that passed eastward either over or to the north of the FASINEX site. Variability due to these synoptic-scale atmospheric systems is most energetic at periods between 2 and 10 days in winter, the band where cyclonic variance dominates.

Squared inner coherences (Mooers 1973) of both the clockwise and anticlockwise $\vec{\tau}$ components among the FNOC, ATOLL, and F2 time series (Fig. 3) are large and statistically significant, except for the less-energetic anticlockwise component at higher frequencies. The largest anticlockwise coherence exists between FNOC and F2 $\vec{\tau}$, suggesting that the FNOC product represents this component of the $\vec{\tau}$ field more accu-

were interpolated to the ATOLL grid using bicubic splines for this calculation.

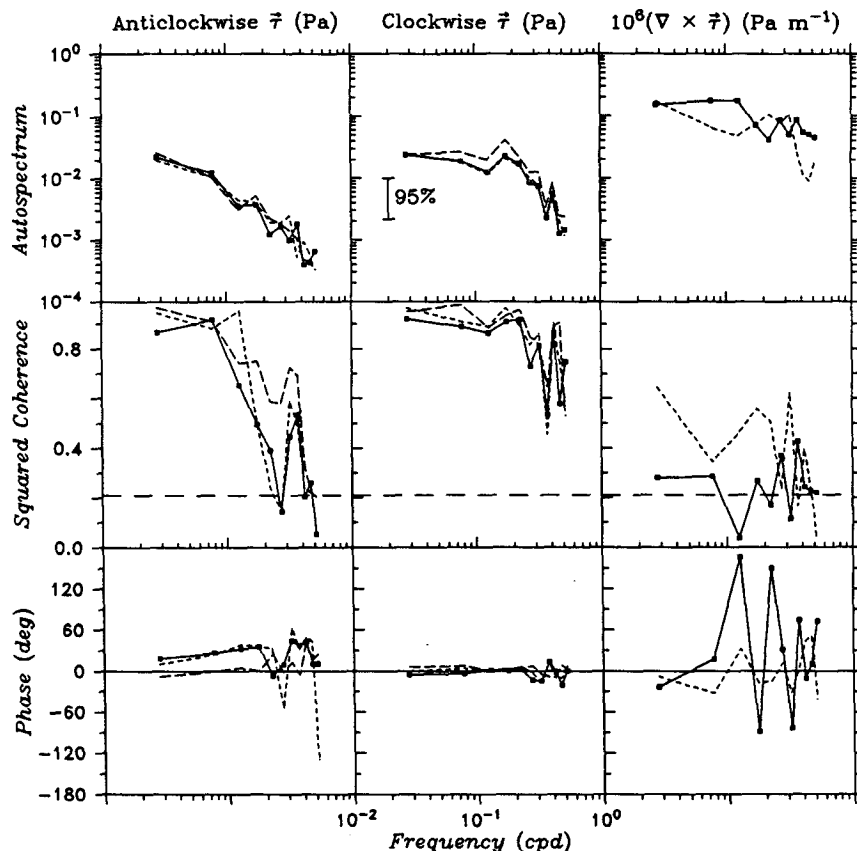FIG. 7. As in Fig. 6 for the ATOLL 5-day $\vec{\tau}$ components.

FIG. 3. Auto- and cross-spectrum analysis of measured and analyzed $\vec{\tau}$ and $\mathbf{k} \cdot \nabla \times \vec{\tau}$ at the FASINEX site, calculated using the 6-h versions of the records plotted in Fig. 2, over the common time interval 18 January through 11 June 1986. Autospectra (top row) of anticlockwise and clockwise $\vec{\tau}$ components are graphed for the ATOLL (solid), FNOC (short dashed), and buoy F2 (long dashed) fields, while autospectra of $\mathbf{k} \cdot \nabla \times \vec{\tau}$ are graphed for the ATOLL (solid) and FNOC (short dashed) fields. Squared inner coherence and phase (middle and bottom rows) of anticlockwise and clockwise $\vec{\tau}$ components are graphed for the FNOC vs ATOLL (solid), F2 vs ATOLL (short dashed), and F2 vs FNOC (long dashed) fields, while squared coherence and phase of $\mathbf{k} \cdot \nabla \times \vec{\tau}$ are graphed for the FNOC vs ATOLL (solid) fields. Also included for comparison are the squared coherence and phase of $\mathbf{k} \cdot \nabla \times \vec{\tau}$ (short dashed) between FNOC grid point (3, 2) and ATOLL grid point (5, 3). The 95% confidence band for autospectra is shown (top center), while the minimum significant squared coherence at 95% confidence is shown by a horizontal dashed line.

rately. Phase is very close to zero for the clockwise component and generally ranges between 0 and 50 degrees for the less-coherent anticlockwise component. Squared coherences between FNOC and ATOLL wind stress curl (Fig. 3) are much lower, and are only significant in 5 of the 11 frequency bands resolved. The corresponding phase estimates therefore vary erratically as a function of frequency. However, we show in the following section that the relationship between FNOC and ATOLL wind stress curl is generally much better than this throughout most of the analysis domain. To illustrate this here in the frequency domain, we present the squared coherence of wind stress curl between FNOC grid point (3, 2) and ATOLL grid point (5, 3) (Fig. 3), which are located about 350 km ESE of the FASINEX site. The coherence is much larger at this

location, being significant in 9 of the 11 frequency bands resolved. Both FNOC and ATOLL analyses represent $\vec{\tau}$ fluctuations very well over the entire frequency band that we resolve, but they represent the wind stress curl fluctuations with somewhat less accuracy.

b. Comparison of the FNOC and ATOLL fields

The correlation coefficients for 6-h u and v between the FNOC and ATOLL fields are about 0.88 throughout the entire analysis domain (not shown). Correlations are also high (0.8–0.9) between the FNOC and ATOLL 6-h $\vec{\tau}$ components everywhere within the domain (Fig. 5), but slightly smaller on average than the correlations for the wind components. The correlations are much smaller for 6-h wind stress curl, with values
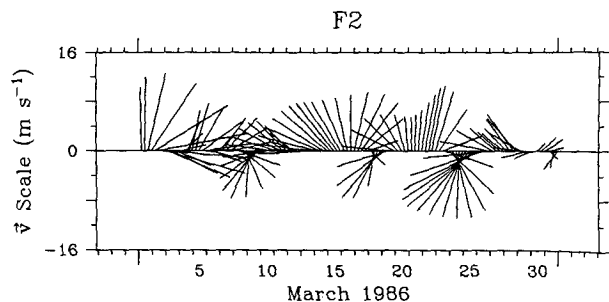
F2

FIG. 4. The surface vector wind measured at FASINEX mooring F2
for March 1986.

< 0.6 over nearly the entire analysis domain. The cor-
relations for 5-day $\vec{\tau}$ components are slightly larger
than those for the 6-h components, with $\tau^{(x)}$ slightly
better correlated than $\tau^{(y)}$ (Fig. 5). The correlations
for 5-day wind stress curl are substantially larger than
those for 6-h curl (Fig. 5), so both analysis fields seem
to represent curl fluctuations with periods longer than
synoptic reasonably well. A minimum in the wind stress
curl correlation exists near the location of the FASI-

FNOC

FIG. 6. Means and rms amplitudes of FNOC $\vec{\tau}$ components over
the time interval 11-15 January through 11-15 May 1986 contoured
within the analysis domain. Dashed contours indicate negative values.

NEX buoys, resulting in the relatively small correlation
between the FNOC and ATOLL 5-day time series
shown in Fig. 2 (0.46) compared to the rest of the
analysis domain (0.6-0.8).

c. Statistical properties

Means and rms amplitudes of the FNOC and
ATOLL $\tau^{(x)}$ and $\tau^{(y)}$ fields (Figs. 6 and 7), and of the

Correlation Coefficients
FNOC vs. ATOLL

FIG. 5. Correlation coefficients between the FNOC and ATOLL
$\vec{\tau}$ components, and between FNOC and ATOLL $\mathbf{k} \cdot \nabla \times \vec{\tau}$, con-
toured within the analysis domain. Correlations for 6-hr (5-day)
variables are contoured in the left (right) panels. The FNOC variables
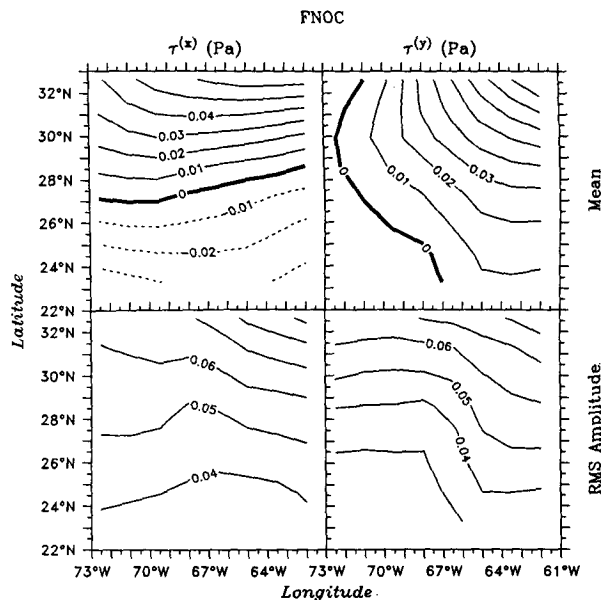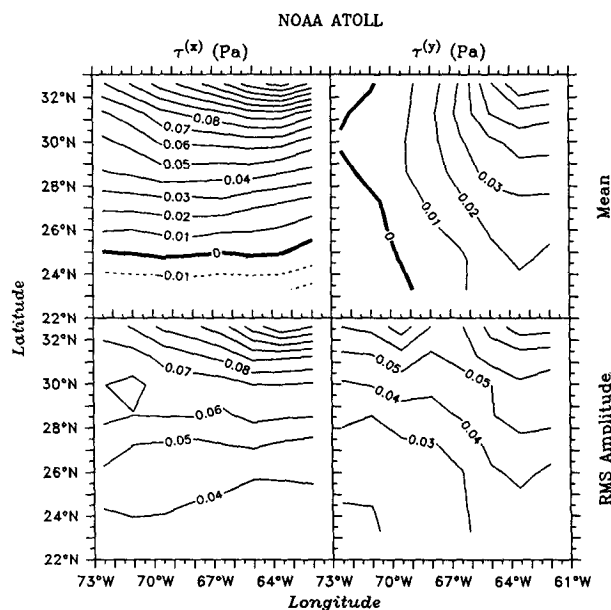were interpolated to the ATOLL grid using bicubic splines for this
calculation.

NOAA ATOLL

FIG. 7. As in Fig. 6 for the ATOLL 5-day $\vec{\tau}$ components.

FNOC and ATOLL wind stress curl fields (Fig. 8), are calculated from 5-day averaged time series for the time interval 11–15 January through 11–15 May 1986. This 4-month interval is used for all subsequent analyses of mean winter conditions during FASINEX. The rapid seasonal increase of T_s begins just after this interval (section 4a).

The statistics of $\tau^{(y)}$ are very similar for the two wind analyses, but this is not true for $\tau^{(x)}$ (Figs. 6 and 7). The eastward bias of mean ATOLL $\bar{\tau}$ is evident throughout the domain and it increases in magnitude toward the north. This bias produces a southward displacement of 2°–3° in the latitude where mean $\tau^{(x)}$ is zero (the boundary between the westerlies and the trades) in the ATOLL field relative to the FNOC field. A large difference exists between the two mean wind stress curl fields (Fig. 8), due primarily to the large difference in $-\partial\tau^{(x)}/\partial y$. The mean ATOLL curl is large and negative throughout the northern part of the analysis domain, while the mean FNOC curl becomes positive to the north of 31°–33°N west of 64°W. The rms amplitude of $\tau^{(x)}$ is similar for the two wind analyses in the southern two-thirds of the domain, but the ATOLL fluctuations are considerably more energetic in the northern third. The same is true for the curl fluctuations. The rms amplitude of $\tau^{(y)}$ has similar values throughout the domain for both analyses.

The differences in mean u and $\tau^{(x)}$ between the FNOC and ATOLL fields probably exist because ATOLL analyses are intended to represent 850 mb winds, while FNOC analyses are intended to represent 19.5 m winds. For both u and $\tau^{(x)}$, the difference is a vector field that points approximately eastward throughout the analysis domain, consistent with a thermal wind balance between a mean eastward wind shear and a mean southward temperature gradient in the planetary boundary layer.

Averages of the $\bar{\tau}$ field over long time intervals are probably more accurate in the FNOC analyses for several reasons: Monthly mean wind stress vectors from the Comprehensive Ocean-Atmosphere Data Set (COADS) (Woodruff et al. 1987) indicate that the zero $\tau^{(x)}$ contour is located between 27° and 28°N on average between January and April (Sadler et al. 1987), which agrees closely with the observed mean FNOC $\tau^{(x)}$ pattern during FASINEX. The mean $\bar{v}$ and $\bar{\tau}$ at the FASINEX buoys are closer to the FNOC means than the ATOLL means (Table 3, Fig. 2). The sign of mean FNOC wind stress curl changes in the northwest part of the analysis domain (Fig. 8). The sign change in this region is also observed in four-year mean fields calculated from European Centre for Medium-Range Weather Forecasts (ECMWF) analyses (Mac Veigh et al. 1987). The large negative mean ATOLL curl observed near 32°N (Fig. 8) is not present in the four-year mean ECMWF field. For these reasons, we chose to use the FNOC analyses in all of our subsequent calculations.

4. The T_s field

a. Quality evaluation

We evaluate the quality of the T_s fields derived from satellite images by comparing time series from the six T_s grid points closest to the FASINEX buoys (Tables 1 and 2) directly with the buoy measurements. Comparisons are made between the individual buoys and the nearest T_s grid points, and between measured time series averaged over all five buoys and the satellite-derived time series averaged over all six grid points. We confine these analyses to the 4-month time interval.

Since image compositing (selecting the warmest pixel) was used as part of the cloud detection procedure, a warm bias in the 5-day T_s maps was expected, and it averages about 0.5–0.6°C near the FASINEX site (Table 5). To understand the effects of compositing on our T_s maps, we created 5-day maximum T_s time series at the FASINEX buoys by selecting the maximum temperature over each 5-day interval instead of averaging. The means of these time series at the buoys are very close to the means at the T_s grid points, indicating that image compositing is the dominant cause of the observed bias. The composited maps also tend to overestimate the rms amplitudes of the fluctuations (Table 5).

The bias between satellite-derived and measured T_s can be tracked as a function of time in Fig. 9, where we plot satellite-derived T_s averaged over the six grid

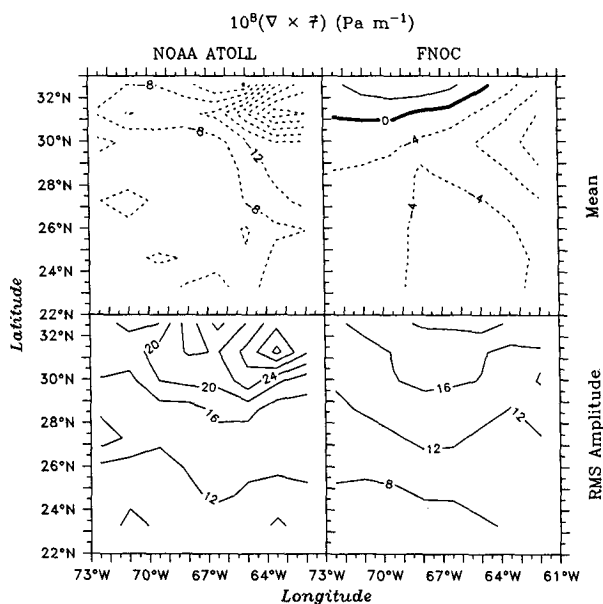$$10^8(\nabla \times \bar{\tau}) \ (\text{Pa m}^{-1})$$

FIG. 8. Means and rms amplitudes of the ATOLL and FNOC 5-day $\mathbf{k} \cdot \nabla \times \bar{\tau}$ over the time interval 11–15 January through 11–15 May 1986 contoured within the analysis domain. Dashed contours indicate negative values.

TABLE 5. Statistics of T_s at the six grid points closest to the FASINEX buoys, and statistics of both 5-day and 5-day maximum T_s time series at the FASINEX buoys, calculated over the time interval 5–9 February to 11–15 May that is both common to all time series and prior to the onset of rapid seasonal warming.

Buoy/grid point	Mean (°C)	Rms amplitude (°C)
T_s (11, 18)	24.65	0.63
T_s (12, 18)	24.63	0.59
T_s (13, 18)	24.65	0.61
T_s (11, 19)	24.62	0.70
T_s (12, 19)	24.62	0.62
T_s (13, 19)	24.53	0.59
F2 (5-day)	24.01	0.53
F4 (5-day)	24.06	0.53
F6 (5-day)	24.01	0.51
F8 (5-day)	24.11	0.51
F10 (5-day)	24.02	0.60
F2 (5-day max)	24.67	0.82
F4 (5-day max)	24.50	0.59
F6 (5-day max)	24.67	0.73
F8 (5-day max)	24.77	0.75
F10 (5-day max)	24.73	0.83

points and 5-day measured T_s averaged over the five FASINEX buoys. The magnitude of the bias varies as a function of time, ranging from about 0.20° to 1.25°C. Diurnal warming events (Stramma et al. 1986) are likely a major cause of the observed temperature bias. These events are weakest in winter and strongest in summer (Cornillon and Stramma 1985), so we expect this influence to increase with time during our analysis interval. For example, it could be responsible for the relatively large bias that existed between late April and early May. Despite the presence of the bias, the major fluctuation events in the FASINEX measurements are reproduced by the satellite-derived data (Fig. 9), but with a somewhat larger amplitude. The rapid seasonal warming clearly begins at the middle of May. The 5-day maximum T_s series averaged over the five buoys follows the satellite-derived data averaged over the six points very closely as a function of time (Fig. 9), indicating again that image compositing is primarily responsible for the bias.

We test whether this bias significantly affects the observed large-scale T_s spatial variability by comparing T_s obtained from three XBT cross sections of the STCZ to satellite-derived T_s along the same track in Fig. 10. The approximate track (about 30.5°N, 70°W to 26°N, 68.5°W) is illustrated in Fig. 1, and the satellite-derived T_s cross section has been spatially interpolated to this track from the unsmoothed 5-day T_s maps using two-dimensional cubic splines. Although the bias is evident, and although there is some disagreement between these two temperature curves for smaller-scale features, reasonably good agreement seems to exist for larger-scale features. The satellite-derived T_s maps are thus reasonably accurate for analyzing large-scale variability only.

Correlation coefficients between 5-day time series at the FASINEX buoys and satellite-derived time series at the nearest grid points range from 0.65–0.84 (Table 6). The correlations are somewhat larger (0.73–0.91) if 5-day maximum time series from the buoys are used. The correlations between T_s time series averaged over the six grid points and both 5-day and 5-day maximum T_s time series averaged over the five buoys (all graphed in Fig. 9) are 0.72 and 0.87, respectively. These correlations are significant, but they are smaller than those observed in the wind and wind stress intercomparison (section 3a).

We explore the reasons for this reduced correlation by calculating correlation coefficients of T_s between F2 and the other FASINEX buoys using both 5-day and 5-day maximum time series. These correlations are surprisingly small, being similar in magnitude to the correlations observed between satellite-derived and measured T_s (Table 6). The T_s variability with space scales smaller than the typical spacing between the buoys (≈ 10 km), such as that due to surface temperature fronts (Weller et al. 1989), could be partly responsible for reducing the correlation among the buoys. This implies that satellite-derived T_s maps may represent large-scale variability more accurately than is implied by the correlation between satellite-derived and measured T_s.

We conclude that the satellite derived T_s field is sufficiently accurate for our analyses of the large-scale T_s variability. However, improvements in the data pro-

Buoys F2–F10 Average T_s (solid)

Buoys F2–F10 Average 5-day Maximum T_s (short dashed)
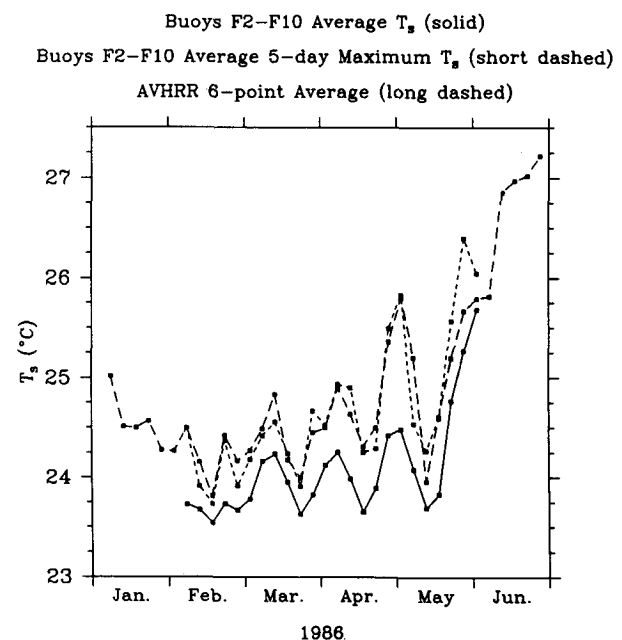
AVHRR 6-point Average (long dashed)

FIG. 9. Time series of 5-day T_s (solid) and 5-day maximum T_s (short-dashed) averaged over buoys F2, F4, F6, F8, and F10, and satellite-derived T_s (dashed) averaged over the six nearest T_s grid points (Table 2).
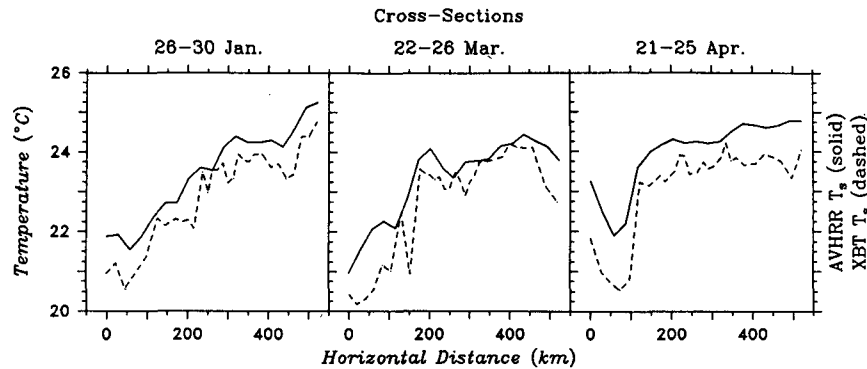
FIG. 10. Cross sections of T_s measured in three ship-of-opportunity XBT cross sections (dashed lines) along the path shown in Fig. 1, and of satellite-derived T_s from unsmoothed 5-day maps (solid lines) interpolated to the same path. The northern part of the path is toward the left.

cessing procedure, such as the reliance on night passes only coupled with improved cloud detection procedures that do not discard as much good data, should improve the quality of the T_s fields in future studies.

b. T_s maps

A typical 5-day T_s map, the one for 31 January through 4 February 1986, is presented in Fig. 11. Although the 0.25° averaging of the composite 5-day images substantially smooths the surface temperature fronts, they can still be identified as bands roughly 50

km wide where the isotherms are relatively densely packed. The strongest front is oriented SW–NE from about 27°N, 72°W to 30°N, 67°W. This front weakens substantially to the east and its path is difficult to follow between 67° and 63°W. Several other frontal bands can be identified in other parts of the analysis domain. The observed temperature bias does not appear to affect the ability to detect these frontal bands. Several regions typically 100–200 km in extent exist where T_s is very uniform.

The T_s maps contain substantial variability with wavelengths $\leq$ 100 km, which cannot be followed coherently from map to map, partly because of noise present in the maps and partly because this variability is dominated by periods $\leq$ 10 days (Leetmaa and

TABLE 6. Correlation coefficients among T_s time series at the six T_s grid points closest to the FASINEX buoys, the time series of T_s averaged over these 6 points, and the T_s time series (both 5-day and 5-day maxima) at the FASINEX buoys. For comparison, correlation coefficients among FASINEX buoys are also presented. These correlations are calculated over the time interval 5–9 Feb. to 11–15 May that is both common to all time series and prior to the onset of rapid seasonal warming.

| Series 1	Series 2	Correlation coefficient
T_s (11, 20)	F2 (5-day)	0.67
T_s (12, 19)	F4 (5-day)	0.72
T_s (11, 19)	F6 (5-day)	0.66
T_s (13, 19)	F8 (5-day)	0.65
T_s (13, 20)	F10 (5-day)	0.84
T_s (6-pt. avg)	F2–F10 Avg (5-day)	0.72
T_s (11, 20)	F2 (5-day max)	0.77
T_s (12, 19)	F4 (5-day max)	0.73
T_s (11, 19)	F6 (5-day max)	0.78
T_s (13, 19)	F8 (5-day max)	0.91
T_s (13, 20)	F10 (5-day max)	0.86
T_s (6-pt. avg)	F2–F10 Avg (5-day max)	0.87
F2 (5-day)	F4 (5-day)	0.67
F2 (5-day)	F6 (5-day)	0.77
F2 (5-day)	F8 (5-day)	0.66
F2 (5-day)	F10 (5-day)	0.64
F2 (5-day max)	F4 (5-day max)	0.72
F2 (5-day max)	F6 (5-day max)	0.94
F2 (5-day max)	F8 (5-day max)	0.76
F2 (5-day max)	F10 (5-day max)	0.71
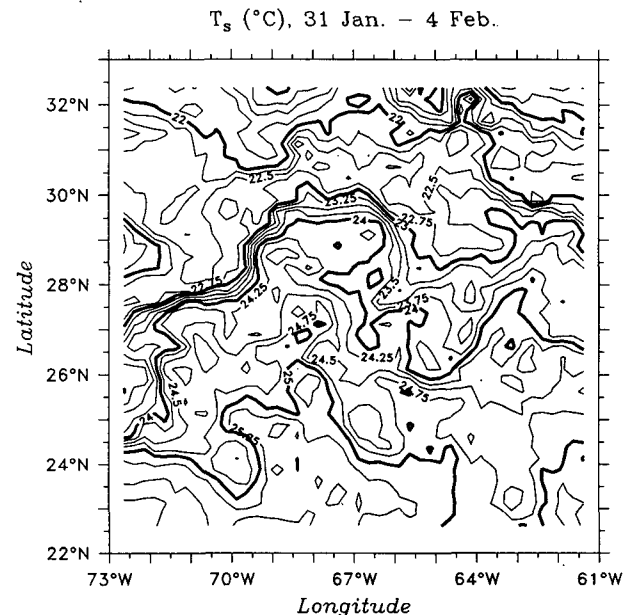
FIG. 11. The 5-day satellite-derived T_s map for 31 January through 4 February 1986.

Voorhis 1978; Voorhis and Bruce 1982). This smaller-scale variability is also poorly correlated spatially between the AVHRR and XBT T_s cross sections in Fig. 10. Further smoothing was therefore required to produce T_s maps that primarily represented the larger-scale variability that could be resolved. We first temporally averaged the 5-day T_s maps over 25-day intervals, which effectively smoothed out most of the smaller-scale variability. To quantify the degree of smoothing achieved, we first calculated meridionally-averaged zonal wavenumber autospectra from the first 25-day map (11–15 January to 31 January–4 February). We then calculated the same autospectra for each of the individual five 5-day maps used to calculate the 25-day map and averaged them together. The ratio of the 25-day to the averaged 5-day spectrum estimates (Table 7) quantifies the variance reduction at each wavenumber due to the temporal averaging. This reduction increases with decreasing wavelength, from 25% at a wavelength of 568 km to >75% for wavelengths ≤ 100 km. Fronts have consequently been substantially smoothed in the 25-day T_s maps (Fig. 12) to the extent that only strong large-scale frontal bands can be easily detected visually.

c. Statistical properties

Between 25° and 30°N, contours of T_s averaged between 11–15 January and 11–15 May 1986 (Fig. 13) are oriented roughly E–W to the east of 68°W, and they are oriented SW–NE to the west of 69°W. A northeastward bulge in the T_s contours is evident near 69°W, covering the FASINEX moorings. This bulge can be identified in the first five 25-day maps in Fig. 12. Halliwell and Cornillon (1989) showed that this bulge was caused by a warm T_s spatial anomaly feature that propagated westward at roughly 2–3 km day^{-1} during the 4-month interval, travelling a total distance of less than half of its zonal size during that time interval. The rms amplitude of T_s (Fig. 13) averages around 0.5°–0.6°C across the entire analysis domain, and there is no apparent organized large-scale structure to this field.
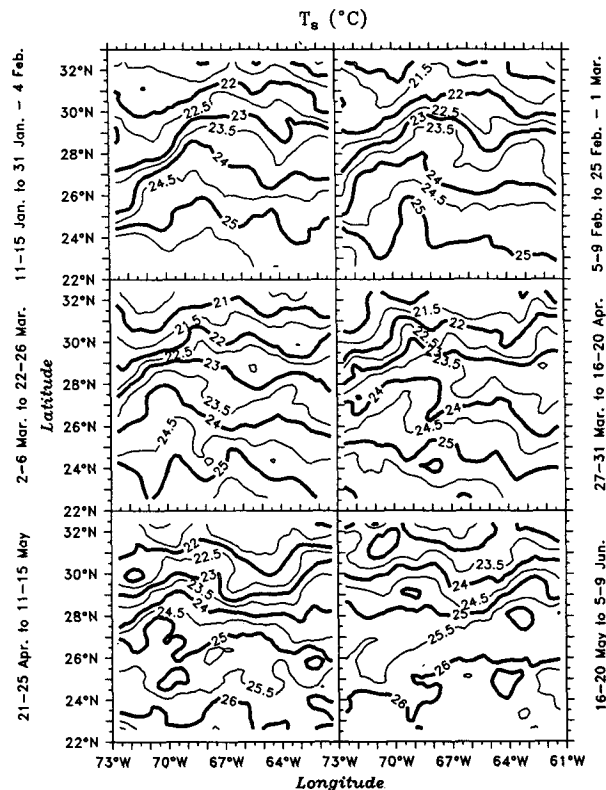

FIG. 12. Maps of the satellite-derived T_s field averaged over six 25-day intervals.

In the mean T_s field, isotherms are packed relatively close together within a predominantly zonally oriented band that crosses the entire domain. We assume that this band, which is clearly evident in the $|\nabla T_s|$ field (Fig. 13), is a realization of the large-scale climatological frontal zone expected to exist within the STCZ, and within which strong subtropical fronts are expected to be found. It will consequently be referred to as the subtropical frontal zone (SFZ). The distinction between frontal zones and fronts is discussed in general by Fedorov (1983), for the North Pacific SFZ by Roden (1980) and Niiler and Reynolds (1984), and for the western North Atlantic SFZ by Halliwell and Cornillon (1989) and Halliwell (1989).

From the 4-month averaged $|\nabla T_s|$ field (Fig. 13), the mean SFZ is centered between 29° and 30°N to the east of 69°W, while it shifts southward with increasing zonal distance to the west of 69°W, reaching about 28°N near 72°W. The mean N–S T_s gradient was 4.2×10^{-6} °C m^{-1} during the 4-month interval, and since values of $|\nabla T_s| > 12 \times 10^{-6}$ °C m^{-1} are outlined by the contours in Fig. 13, the regions where mean gradients exceed about three times the mean N–S gradient are essentially outlined in this plot. Using this criterion to define the boundaries of the SFZ, it is up to 3 degrees latitude wide. The path of the mean

TABLE 7. The ratios of zonal wavenumber autospectrum estimates from a 25-day T_s map (11–15 January to 31 January–4 February) to averaged estimates from the five 5-day maps used to construct the 25-day T_s map.

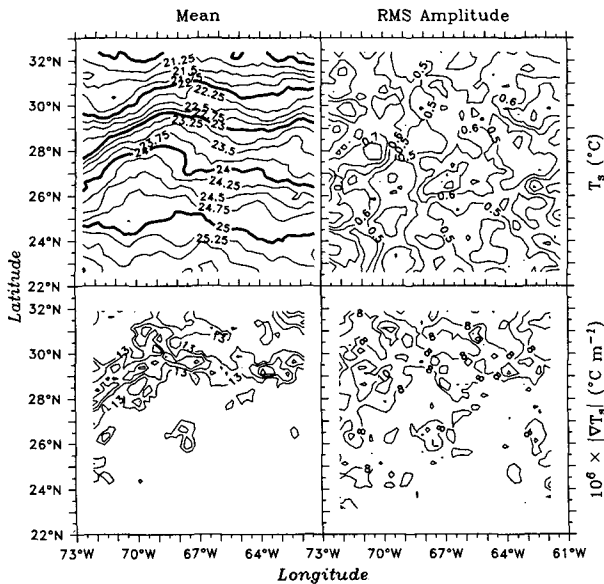| Zonal wavelength (km)	Spectrum estimates		Ratio
	25-day	Averaged 5-day	
568	1526	2057	0.74
227	174	364	0.48
142	40.7	123	0.33
103	15.5	68.6	0.23
81	10.4	44.8	0.23
67	7.00	32.5	0.22

FIG. 13. Means and rms amplitudes of T_s (top) and $|\nabla T_s|$ (bottom) over the time interval 11–15 January through 11–15 May 1986 contoured within the analysis domain. Values of T_s are biased high by about 0.5°–0.6°C throughout the domain as described in Section 4a. Only $|\nabla T_s|$ values over 1.3×10^{-5} °C m^{-1} are contoured. Dashed contours indicate negative values.

and the latitude at which this maximum value occurred at eight separate longitudes as a function of time (Fig. 15). West of 70°W, the SFZ shifts rapidly northward during January and February. In the first 25-day interval, the SFZ is centered near 25°N at the western end of the analysis domain, but shifts northward to near 28°N by early March. The SFZ meanders southward between 66° and 63°W during February and March, and it shifts northward east of 63°W during April. The most intriguing result of this analysis, however, is the apparent westward propagation of maxima and minima in $|\nabla T_s|_{max}$ (Fig. 15). The largest values of $|\nabla T_s|_{max}$ are observed between 69° and 72°W, and there is a slight indication of westward propagation for this maximum at an average speed of about 1 km day^{-1}. East of 69°W, there is clearer evidence of westward propagation, with both a maximum and a minimum in $|\nabla T_s|_{max}$ propagating westward at about 4 km day^{-1}. Westward propagation is not visually evident in the latitude of the SFZ. We therefore see no clear evidence for the propagation of SFZ meanders (although the space–time coverage of this dataset is too small to conclude this absolutely), but we do see
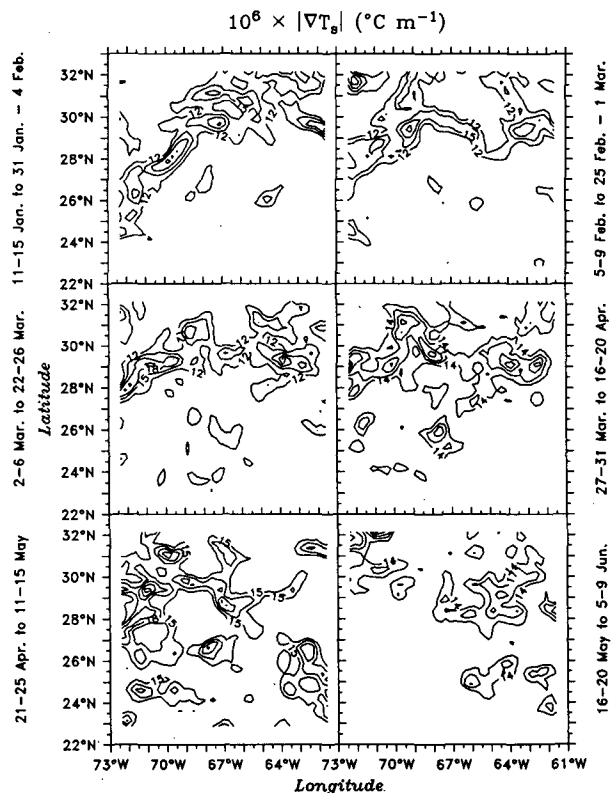
SFZ does not follow a particular isotherm. It is centered near the 23.25°C (22.75°C) isotherm at the western (eastern) end of the domain. The rms amplitude of $|\nabla T_s|$ (Fig. 13) tends to be larger within the SFZ than elsewhere in the analysis domain.

The width of the SFZ and the magnitude of T_s gradients within the SFZ depend in part on the degree of smoothing in the T_s maps. Consequently, we focus only on the space–time variability of the SFZ in our subsequent analyses. White et al. (1978) has discussed the appropriateness of using smoothed data to characterize the large-scale variability of the western North Pacific SFZ.

d. Strength and location of the SFZ

We calculate and contour $|\nabla T_s|$ maps (Fig. 14) from the 25-day average T_s maps shown in Fig. 12. The SFZ is irregular in strength and shape, but it can be followed zonally across most of the northern part of the domain in all 25-day averages, becoming more broken by the final 25-day interval when rapid seasonal warming was occurring.

Since the $|\nabla T_s|$ field in Fig. 14 is strongly affected by smaller-scale variability, we recalculated these $|\nabla T_s|$ maps using 25-day T_s maps smoothed with a 9 × 9 point (2° × 2°), two-dimensional Hanning window (Part II) to focus on the large-scale variability of the SFZ. Using these smoothed 25-day maps (not shown), we recorded both the maximum value of the temperature gradient magnitude ($|\nabla T_s|_{max}$) within the SFZ

$$10^6 \times |\nabla T_s| \ (\text{°C m}^{-1})$$

FIG. 14. Temperature gradient magnitude ($|\nabla T_s|$) calculated from the 25-day averaged T_s maps in Fig. 12 and contoured over the analysis domain. Only gradient magnitudes greater than a certain threshold value are contoured. The threshold values are set separately for each plot to best outline the SFZ while minimizing the clutter due to small-scale regions of relatively large $|\nabla T_s|$.
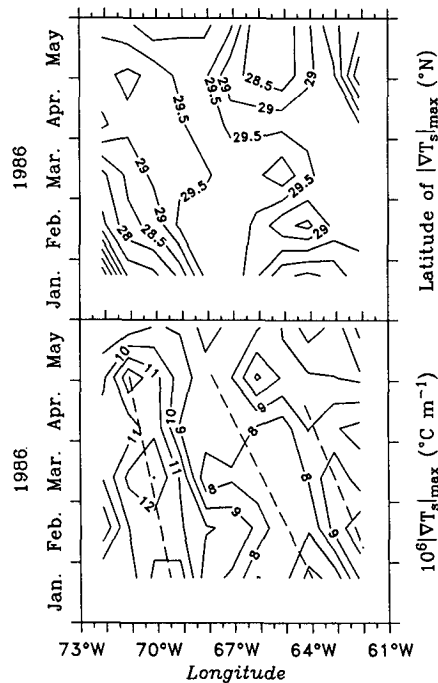
FIG. 15. The latitude (top) and the maximum temperature gradient magnitude ($|\nabla T_s|_{max}$) (bottom) of the SFZ contoured as a function of longitude and time. Propagation of extrema in the maximum gradient magnitude is indicated by dashed lines.

evidence for westward propagation of perturbations in the strength of the SFZ.

The causes of this westward propagation are explored further in three follow-on studies (Part II; Halliwell and Cornillon 1989; Halliwell 1990). The large-scale westward-propagating T_s spatial anomaly features that influenced the spatial pattern of mean T_s during FA-SINEX (section 4c) were apparently responsible for much of the observed variability in T_s and the SFZ that occurred between mid-January and mid-May 1986. These studies suggest (but do not prove conclusively) that these large-scale anomaly features and the associated SFZ variability could result from a mixed-layer response to the underlying internal eddy field at wavelengths of several hundred kilometers. Wind-driven horizontal heat advection in the Ekman layer could not account for the existence of these anomaly features. Halliwell and Cornillon (1989) describe the relationship between the SFZ and these propagating features.

5. Discussion

This study was designed to describe the basic statistical properties of the large-scale $\vec{\tau}$ and T_s fields, and the large-scale space–time variability of the subtropical frontal zone (SFZ), during FASINEX (January through June 1986). It was also intended to evaluate the quality of the FASINEX large-scale dataset.

Time series of 6-h and 5-day $\vec{\tau}$ calculated from both the FNOC and NOAA ATOLL wind analysis fields were highly correlated (near 0.9) over the entire analysis domain. Time series of wind stress curl were less well correlated, equalling 0.6–0.8 for the 5-day time series. Spectral shapes of the $\vec{\tau}$ time series measured at the FASINEX site were accurately reproduced by both $\vec{\tau}$ analyses over the entire frequency band that we could resolve during FASINEX (0.028–0.5 cpd), and these series were highly coherent. The clockwise component of $\vec{\tau}$ was an order of magnitude more energetic than the anticlockwise component at the FASINEX site at frequencies $\geq$ 0.1 cpd. The energy levels were nearly the same at lower frequencies.

Although both wind analyses represented synoptic-scale atmospheric fluctuations quite well, longer-term averages of u, $\tau^{(x)}$, and $\mathbf{k} \cdot \nabla \times \vec{\tau}$ were represented best by the FNOC analyses. The ATOLL (FNOC) analyses are intended to represent the 850 mb (19.5 m) wind field, and the mean ATOLL wind and wind stress vectors are apparently influenced by the mean eastward atmospheric wind velocity shear between the surface and 850 mb due to the thermal wind balance with a mean southward atmospheric temperature gradient.

Large-scale variability in the T_s field was fairly well represented by the satellite-derived T_s maps, but a mean bias of +0.5°–0.6°C existed within the analysis domain. We derived our T_s maps from 5-day composite AVHRR images formed by selecting the warmest temperature at each pixel within each 5-day interval to eliminate most of the cloud contamination. The bias probably arose from the influence of diurnal warming due to the inclusion of both day and night images in the composites. This bias did not obscure the large-scale T_s variability in the maps, nor did it hinder the detection of frontal zones, so the maps represented the T_s variability sufficiently well for the purposes of this study.

To study the basic statistical properties of the T_s field at large horizontal scales, we further averaged the T_s maps over 25-day intervals, which suppressed most of the spatial variability at wavelengths $\leq$ 200–250 km. One of the dominant large-scale features observed in these 25-day maps was a predominantly zonal frontal band (the SFZ) that stretched across the entire analysis domain. Perturbations in the strength of the SFZ as a function of longitude were observed to propagate westward with time.

We continue our analyses in Part II by describing the response of T_s and of the SFZ to wind-driven horizontal heat advection using the dataset described in this paper. Also, the question of westward propagation that arose in our basic statistical description of the SFZ prompted us to study the large-scale T_s anomalies associated with the SFZ (Halliwell and Cornillon 1989; Halliwell 1990). In these studies, we show that the observed SFZ propagation is associated with large-scale westward-propagating T_s anomaly features, then ana-

lyze possible forcing mechanisms for these features. The extent to which these observed properties are characteristic of the western North Atlantic STCZ or peculiar to the FASINEX period will need to be determined by analyzing a much longer dataset.

REFERENCES

Cornillon, P., and L. Stramma, 1985: The distribution of diurnal sea surface warming events in the western Sargasso Sea. *J. Geophys. Res.*, **90**, 11 811–11 815.
——, C. Gilman, L. Stramma, O. Brown, R. Evans and J. Brown, 1987: Processing and analysis of large volumes of satellite-derived thermal infrared data. *J. Geophys. Res.*, **92**, 12 993–13 002.
Evans, D. L., G. A. Strout and A. K. Monaghan, 1986: FASINEX ship-of-opportunity data report. Tech. Rep. Ref. No. 86-6, Graduate School of Oceanography, University of Rhode Island, Narragansett, Rhode Island.
Fedorov, N. K., 1983: The physical nature and structure of oceanic fronts. *Lect. Notes on Coast. and Estuar. Stud.*, **19**, N. Demidenko, Translator, C. Garrett, Tech. Ed., Springer-Verlag, 333 pp.
Friehe, C. A., and S. E. Pazan, 1978: Performance of an air-sea interaction buoy. *J. Appl. Meteor.*, **17**, 1488–1497.
Halliwell, Jr., G. R., 1990: Ship-of-opportunity XBT cross-sections of the western North Atlantic subtropical convergence zone. *J. Geophys. Res.*, in press.
——, and J. S. Allen, 1987: The large-scale coastal wind field along the west coast of North America, 1981–1982. *J. Geophys. Res.*, **92**, 1861–1884.
——, and P. Cornillon, 1987: Five-day maps of AVHRR/2 sea surface temperature fields and wind stress analysis during FASINEX. Tech. Rep. 87-5, Graduate School of Oceanography, University of Rhode Island, Narragansett, R.I., 67 pp.
——, and ——, 1989: Large-scale SST anomalies associated with subtropical fronts in the western North Atlantic during FASINEX. *J. Mar. Res.*, in press.
——, and ——, 1990: Large-Scale SST Variability in the western North Atlantic subtropical convergence zone during FASINEX, Part II: Upper ocean heat balance and frontogenesis. *J. Phys. Oceanogr.*, **20**, 223–234.

——, H. L. Pittock, V. M. Halliwell and J. S. Allen, 1986: The CODE large-scale meteorological, sea surface temperature, and coastal sea level data set, 1980–84. Ref. 86-15, Data Rep. 125, College of Oceanography, Oregon State University, Corvallis, OR, 442 pp.
Large, W. G., and S. Pond, 1981: Open ocean flux measurements in moderate to strong winds. *J. Phys. Oceanogr.*, **11**, 324–336.
Leetmaa, A., and A. D. Voorhis, 1978: Scales of motion in the subtropical convergence zone. *J. Geophys. Res.*, **83**, 4589–4592.
Lewis, J. M., and T. H. Grayson, 1972: The adjustment of surface wind and pressure by Sasaki's variational matching technique. *J. Appl. Meteor.*, **11**, 586–597.
Mac Veigh, J. P., B. Barnier and C. Le Provost, 1987: Spectral and empirical orthogonal function analysis of four years of European Center for Medium-Range Weather Forecast wind stress curl over the North Atlantic Ocean. *J. Geophys. Res.*, **92**, 13 141–13 152.
Mooers, C. N. K., 1973: A technique for the cross-spectrum analysis of pairs of complex-valued time series, with emphasis on properties of polarized components and rotational invariants. *Deep-Sea Res.*, **92**, 1129–1141.
Niiler, P. P., and R. W. Reynolds, 1984: The three-dimensional circulation near the eastern North Pacific subtropical front. *J. Phys. Oceanogr.*, **14**, 217–230.
Pennington, N. J., R. A. Weller and K. H. Brink, 1988: FASINEX moored current meter array data report. WHOI Tech. Rep. 88-63, Woods Hole Oceanographic Institution, Woods Hole, MA.
Roden, G. I., 1975: On North Pacific temperature, salinity, sound velocity, and density fronts and their relation to the wind and energy flux fields. *J. Phys. Oceanogr.*, **5**, 557–571.
——, 1980: On the subtropical frontal zone north of Hawaii during winter. *J. Phys. Oceanogr.*, **10**, 342–362.
Sadler, J. C., M. A. Lander, A. M. Hori and L. K. Oda, 1987: *Tropical Marine Climate Atlas, Vol. 1: Indian and Atlantic Oceans.* Tech. Rep. UHMET 87-01, Department of Meteorology, University of Hawaii, Honolulu, Hawaii.
Stage, S. A., and R. A. Weller, 1985: The Frontal Air–Sea Interaction Experiment (FASINEX). Part I: Background and scientific objectives. *Bull. Amer. Meteor. Soc.*, **66**, 1511–1520.
——, and ——, 1986: The Frontal Air–Sea Interaction Experiment (FASINEX). Part II: Experimental plan. *Bull. Amer. Meteor. Soc.*, **67**, 16–20.
Stramma, L., P. Cornillon, R. A. Weller, J. F. Price and M. G. Briscoe, 1986: Large diurnal sea surface temperature variability: Satellite and in situ measurements. *J. Phys. Oceanogr.*, **16**, 827–837.
Van Woert, M. L., 1982: The subtropical front: Satellite observations during FRONTS 80. *J. Geophys. Res.*, **87**, 9523–9536.
Voorhis, A. D., 1969: The horizontal extent and persistence of thermal fronts in the Sargasso Sea. *Deep-Sea Res.*, **16**(Suppl.), 331–337.
——, and J. G. Bruce, 1982: Small-scale surface stirring and frontogenesis in the subtropical convergence of the western North Atlantic. *J. Mar. Res.*, **40**(Suppl.), 801–821.
Weller, R. A., J. Dean, D. Rudnick, N. J. Pennington, R. Trask, J. Valdes and R. Payne, 1990: Measuring local meteorology and upper-ocean variability at an array of surface moorings in the subtropical convergence zone. *J. Atmos. Oceanic Technol.*, **7**, in press.
White, W. B., K. Hasunuma and H. Solomon, 1978: Large-scale seasonal and secular variability of the subtropical front in the western North Pacific from 1954 to 1974. *J. Geophys. Res.*, **83**, 4531–4544.
Woodruff, S. D., R. J. Slutz, R. L. Jenne and P. M. Steurer, 1987: A comprehensive ocean-atmosphere data set. *Bull. Amer. Meteor. Soc.*, **68**, 1239–1250.